Please do not adjust margins

ARTICLE

Oxygen-Vacancy–Driven Stabilization of Tetragonal ZrO_2

Zi-Zhan He[a], Teng-Fei Li[a], Lin Chen[a], Zhi-Pan Liu[a,b]*, Cheng Shang[a]*

Received 00th January 20xx,
Accepted 00th January 20xx

DOI: 10.1039/x0xx00000x

The tetragonal phase of zirconium dioxide (t-ZrO_2) has wide applications in catalysis, ceramics, and ferroelectrics, yet its stabilization under mild conditions remains elusive. Here we employ global potential energy surface exploration accelerated by global neural network potentials to resolve its atomistic origin. We demonstrate that chemical additives stabilize t-ZrO_2 by introducing a specific spatial distribution of formal oxygen vacancies, while oxygen-deficient ZrO_{2-x} at certain vacancy concentrations ($0.12 < x \leq 0.31$) also favors the tetragonal phase intrinsically. Electronic structure analysis reveals that vacancy–vacancy interaction states inject electrons into the band gap and lower the energy difference between monoclinic and tetragonal phases. Driven by this fundamental insight, we introduce a quantitative descriptor to map the stabilization potential across the periodic table, successfully guiding the a priori prediction and experimental realization of previously unreported MZrO solid solutions. Our results establish oxygen vacancy concentration as the central design principle for making t-ZrO_2 and provide a general framework for tailoring defect-driven stability in functional oxides.

1. Introduction

The tetragonal phase of zirconium dioxide (t-ZrO_2) attracts sustained interest owing to its non-toxicity and outstanding mechanical properties, including high strength and hardness. These attributes facilitate its widespread applications in catalysis[1–3] and ceramics[4–7]. However, bulk t-ZrO_2 is thermodynamically stable only at high temperatures (1175–2370 °C) and undergoes a spontaneous transformation to monoclinic ZrO_2 (m-ZrO_2) upon cooling to room temperature.[8] Considerable efforts are therefore devoted to synthesizing nanosized t-ZrO_2 under mild conditions,[9–13] among which the use of alkaline additives in hydrothermal processes and the application of organic zirconium alkoxides are widely recognized as the most effective approaches, yielding stable 3–13 nm particles that withstand calcination up to 700 °C[11,12]. Despite these empirical successes, the fundamental mechanisms responsible for stabilizing the tetragonal phase under different synthesis conditions remain elusive.

Three main mechanisms are proposed for stabilizing t-ZrO_2: (i) surface effects[14], (ii) structural effects induced by doping[15,16], and (iii) oxygen vacancies[17–19]. Garvie originally attributes t-ZrO_2 stabilization to surface effects, suggesting a critical particle size of ~15 nm[14]. However, subsequent DFT studies by Piskorz show that both clean and hydroxylated m-ZrO_2 surfaces are more stable than t-ZrO_2[20,21], indicating that surface effects alone cannot fully account for the observed stabilization. Doping effects are well established for Y- and Ce-doped systems, yet they fail to explain stabilization in Na- and Ca-doped systems[15,16,22,23], where structurally distinct Na_2O (anti-fluorite) and CaO (rock-salt) still promote the tetragonal phase[9–11]. Moreover, the successful synthesis of dopant-free t-ZrO_2 confirms that chemical doping is not an indispensable condition. While these traditional macroscopic factors (e.g., surface energy, grain size, and chemical doping) are undeniably critical to the observable stability of t-ZrO_2, their individual frameworks sometimes encounter empirical inconsistencies across disparate synthesis routes. This implies that a more fundamental, lower-dimensional physical descriptor might act as the shared underlying driving force behind these diverse macroscopic phenomena.

Closer examination of existing synthesis strategies reveals deeper complexities and subtle constraints. While traditional stabilizers like Ce and Y require only a minimum threshold concentration,[15,16,22,23] alkaline-assisted synthesis exhibits a peculiar "optimal concentration" effect, such as 10 mol% NaOH or 20 mol% Ca,[9,11,24] suggesting that the stabilizing effect is highly sensitive to the local dopant concentration. Intriguingly, t-ZrO_2 phases synthesized via different methods display comparable thermal stabilities, with the t→m phase transition consistently occurring between 500 and 700 °C during calcination,[11,13,25] implying a shared, route-independent stabilizing mechanism.

Notably, t-ZrO_2 derived from organic precursors often displays a distinct light-brown hue and a narrowed band gap (2.28 eV),[25] characteristics typically attributed to oxygen vacancies (O_v). Photoluminescence spectroscopy also confirms the presence of O_v in samples prepared with $NH_3 \cdot H_2O$.[26] Early theoretical work by Fabris shows that vacancies preferentially localize near Zr, contributing to t-phase stabilization[17], and

[a] *Collaborative Innovation Center of Chemistry for Energy Material, Shanghai Key Laboratory of Molecular Catalysis and Innovative Materials, Key Laboratory of Computational Physical Science, Department of Chemistry, Fudan University, Shanghai 200433, China*
[b] *Key Laboratory of Synthetic and Self-Assembly Chemistry for Organic Functional Molecules, Shanghai Institute of Organic Chemistry, Chinese Academy of Sciences, Shanghai 200032, China*
* Correspondence: zpliu@fudan.edu.cn; cshang@fudan.edu.cn
ORCID: Zhi-Pan Liu, 0000-0002-2906-5217; Cheng Shang, 0000-0001-7486-1514

Please do not adjust margins

Please do not adjust margins

Chang & Doong experimentally confirm their presence via O/Zr ratio measurements[18]. These scattered clues strongly point toward O_v as a crucial, route-independent participant in zirconia thermodynamics. However, these pioneering studies remain descriptive and phenomenological, where the underlying electronic driving force and a quantitative, predictive metric connecting atomic-scale defects to macroscopic stability are still unclear, which is essential for transforming scattered empirical observations into a predictive design principle.

Herein, we employ the stochastic surface walking method combined with the neural network potential (SSW-NN) to uncover the intrinsic physical mechanism of vacancy-driven stabilization. By mapping the thermodynamic convex hulls of NaZrO, KZrO, CaZrO and HZrO systems, we successfully reproduce the experimentally observed stabilization of tetragonal ZrO_2 phases and identify their exact concentration windows. Crucially, we reveal that the specific distribution and bulk coordination behavior of formal oxygen vacancies act as an omnipresent thermodynamic baseline that persists across all conditions, emerging as the decisive force governing phase stability in larger crystal regimes. Guided by this mechanistic insight, we establish a physically transparent, quantitative descriptor based on the propensity of metal oxide dopants to generate O_v within the zirconia lattice. Through a high-throughput screening of over 40 elements, this mechanism-driven descriptor successfully predicts a previously unreported, highly stable IrZrO tetragonal solid solution, which is subsequently validated by experimental synthesis. These findings provide a unified theoretical foundation for the rational design of phase-controlled, zirconia-based functional materials.

2. Computational details

2.1 SSW-NN Simulations

Our approach for resolving the structures of XZrO (X=H, Na, K, Ca) systems and ZrO_{2-x} synthesized by the hydrothermal method is based on the SSW-NN method as implemented in the LASP code.[27–31] The details of the SSW–NN method are provided in Section 1 of the Supporting Information. The machine learning NN potential is generated by iterative self-learning of the plane wave density functional theory (DFT) global PES dataset generated from SSW exploration. The SSW-NN simulation to explore PES can be divided into three steps: global dataset generation based on DFT calculations using selected structures from SSW simulations, NN potential fitting, and SSW global-optimization using NN potential. These steps are iteratively performed until the NN potential is transferable and robust enough to describe the global PES. At first, the global dataset is built iteratively during the self-learning of NN potential.[32–34] The initial data of the global dataset come from the DFT-based SSW simulation and all the other data are taken from NN-based SSW PES exploration. In order to cover all the likely compositions of X-Zr-O systems based on previous work (e.g., Zr metal, XZr alloys, and XZrO composites), SSW simulations are carried out for different structures (including bulk, layer, and cluster), compositions and numbers of atoms per unit cell (Supplementary Information, **Tables S1–S3**). Overall, these SSW simulations generate more than 10^7 structures on PES. The final X-Zr-O training dataset consists of 35,699 structures for CaZrO, 40,582 structures for KZrO and 41,077 structures for NaZrO. Then, the NN potential is generated using the method introduced in our previous work. To pursue high accuracy for PES, we adopt a large set of power-type structure descriptors, which contains 303 descriptors for every element in KZrO, NaZrO and CaZrO and the network utilized is also large involving five hidden layers (321-100-80-80-6 net), equivalent to 140,940 network parameters in total for KZrO and NaZrO and five hidden layers (321-120-80-80-6 net), equivalent to 165,000 network parameters in total for CaZrO. The min-max scaling is utilized to normalize the training data sets. Hyperbolic tangent activation functions are used for the hidden layers, while a linear transformation is applied to the output layer of all networks. The limited-memory Broyden–Fletcher–Goldfarb–Shanno method is used to minimize the loss function to match DFT energy, force, and stress. The final energy and force criteria of the root mean square errors (RMSE) are 5.64 meV per atom and 0.152 eV $Å^{-1}$ for CaZrO, 5.62 meV per atom and 0.166 eV $Å^{-1}$ for KZrO, 5.77 meV per atom and 0.168 eV $Å^{-1}$ for NaZrO, respectively. We perform additional tests to benchmark the reliability of the global minimum (GM) search for these systems. For each XZrO composition, the four most stable structures are selected and calculated using DFT, as summarized in Tables S4a–c. As shown in Fig. S2, the comparison between NN+D3 and DFT+D3 relative energies includes 76 structures across 19 compositions for CaZrO, 64 structures across 16 compositions for NaZrO, and 40 structures across 10 compositions for KZrO. The corresponding R^2 values are 0.93, 0.96, and 0.88, respectively, indicating good agreement between the two methods across these systems. The RMSE of all tested potentials is below 4 meV/atom. Cross-validation is conducted on the CaZrO system as a representative example, using an additional 1000 structures not included in the training set (**Fig. S1**). During training, the RMSE of the training set decreases from approximately 5.80 to 5.63 meV/atom, while the test set RMSE slightly increases from 5.95 to 6.17 meV/atom before plateauing. Force and stress RMSEs for both sets stabilize at around 0.16 eV/Å and 1.8 GPa, respectively. The small and stable gap between training and test errors indicates negligible overfitting, confirming the robustness of the NN potential.

2.2 DFT Calculations

All DFT calculations are performed by using the plane wave VASP code, where electron-ion interaction is represented by the projector augmented wave pseudopotential[35,36]. The exchange functional utilized is the GGA-PBE[37]. The kinetic energy cutoff is set as 450 eV. The first Brillouin zone k-point sampling adopts the Monkhorst−Pack scheme with an automated mesh determined by 25 times the reciprocal lattice vectors (25 $Å^{-1}$). The energy and force criteria for convergence of the electron density and structure-optimization are set at 10^{-6} eV and 0.05 eV·$Å^{-1}$, respectively. The k-point density and force convergence criteria are further benchmarked on the NaZrO system using a k-point density of 35 $Å^{-1}$ and a force convergence threshold of 0.01

 This journal is © The Royal Society of Chemistry 20xx

Please do not adjust margins

Please do not adjust margins

eV, as shown in **Table S4d**. The results indicate that the use of denser k-points and higher convergence criteria leads to an energy difference of less than 0.2 meV/atom. Grimme D3 is utilized to include the long-range van der Waals interaction[38]. In computing the band structures, we employ the HSE06 hybrid functional with the standard exchange mixing containing 25% Hartree–Fock and 75% PBE[39].

2.3 Thermodynamic Data Evaluation

To investigate the stability of the Na_2O-ZrO_2 structures at different temperatures, we calculate the free formation energy per metal atom ΔG_f by referencing the bulk m-ZrO_2 and solid Na_2O using Eq. (1):

$$\Delta G_f = \frac{\left[G\left(Na_{2x}Zr_yO_{x+2y}\right) - xG(Na_2O) - yG(ZrO_2)\right]}{2x+y} \quad (1)$$

where $G(Na_{2x}Zr_yO_{x+2y})$, $G(Na_2O)$, and $G(ZrO_2)$ are the free energies of $Na_{2x}Zr_yO_{x+2y}$, Na_2O, and m-ZrO_2 in the solid phase at different temperatures. We approximate these using the following Eq. (2):

$$G_{solid}(300K) = E_{solid} + ZPE - TS \quad (2)$$

where E_{solid} is the total energy of the solid phase obtained from DFT calculations, ZPE is the zero-point energy, T is the temperature in kelvin, and S is the entropy contribution. The vibrational entropy is approximated using the harmonic oscillator model. The frequencies are calculated using NN potential functions, and the ZPE and S are obtained using the VASPKIT tool[40]. The configurational entropy S_{config} given by Eq. 3 is considered for t-phase ZrO_{2-x} structures containing oxygen vacancies, where R=8.314 $J \cdot mol^{-1} \cdot K^{-1}$ is the gas constant. Ω, which is calculated using Eq. 4, is the number of microstates, representing all possible configurations weighted by the Boltzmann distribution. In Eq. 4, k_b is the Boltzmann constant 1.38×10^{-23} $J \cdot K^{-1}$. E_i is the energy of a given configuration relative to the global minimum.

$$S_{config} = R \ln \Omega \quad (3)$$

$$\Omega(T) = \sum_i e^{-Ei/k_bT} \quad (4)$$

We plot thermodynamic convex hulls for ZrO_{2-x} systems. The GM structures are subjected to DFT and frequency calculations to obtain free energy values at different temperatures.

$$\Delta G_f = \frac{G\{ZrO_{2-x} - N[x \cdot \mu(Zr_2O_3) + (1-x) \cdot \mu(ZrO_2)]\}}{N} \quad (5)$$

where $G(ZrO_{2-x})$ represents the free energy of the ZrO_{2-x} system at a given temperature, N represents the number of ZrO_2 units, $\mu(Zr_2O_3)$ and $\mu(ZrO_2)$ represent the chemical potentials per chemical unit at the same temperature. The adequacy of the harmonic approximation in the 900–1600 K range is further verified by molecular-dynamics sampling based on velocity autocorrelation functions, which reproduces the t–m equilibrium temperature of ZrO_2 to within 25 K of the harmonic result (Table S10 in the Supporting Information).

2.4 Identification of t-like structures

First, the structures obtained from SSW exploration are ranked by energy, and duplicate structures are screened using a descriptor-based similarity criterion[32]. We then retain only structures whose energies fall within the window bounded by those of pristine m-ZrO_2 and t-ZrO_2. Simulated XRD patterns are subsequently calculated for these candidates, and structures exhibiting the characteristic tetragonal reflections at $2\theta \approx 30°$, 35°, 50°, and 60° are selected for the final re-filling check.

The re-filling check is performed to verify that the identified t-like MZrO (M = Na, Ca, K, H) and ZrO_{2-x} structures are indeed derived from t-ZrO_2. Specifically, we first identify the oxygen vacancies in these structures and fill them with oxygen atoms. For MZrO structures, all M atoms are then replaced by Zr atoms. Finally, the resulting structures are fully optimized to local energy minima. If the optimized structure adopts the t-ZrO_2 phase, the original structure is classified as t-like. We note that the re-filling check is a consistency test of the t-ZrO_2 ancestry rather than a unique proof. Because the re-filled configuration retains the atomic topology of the parent structure, local optimization converges to the basin of the parent framework: a non-t structure therefore relaxes back to its own phase and fails the check, whereas a t-derived framework relaxes to t-ZrO_2 unless the vacancy or dopant arrangement has already distorted it beyond the tetragonal basin. Together with the preceding energy-window and XRD-fingerprint filters, the probability of misclassification is therefore substantially reduced, and the RDF analysis of the vacancy distribution (Fig. 2) provides an additional, independent verification.

3. Results

3.1 Phase Stability of Alkali Metal–ZrO_2 Systems

We first employ the SSW-NN method to investigate the thermodynamic phase diagram of Na_2O-ZrO_2 (NaZrO), a representative alkali metal oxide-ZrO_2 system. A series of structures with a number of atoms ranging from 12 to 111 atoms and varying Na^+ contents (0–100%) are sampled. For each stoichiometry, more than 40,000 minima are collected to ensure comprehensive exploration of the potential energy surface and identification of global minimum (GM) structures. **Fig. 1a** presents the resulting thermodynamic convex hull at 1000 K, the characteristic temperature for t-ZrO_2 synthesis via NaOH precipitation. Formation free energies (ΔG_f) are calculated according to Eqs. (1) and (2) (also **Table S5**), with vertex structures (GMs) highlighted in red. The energies and structural data of all GM structures shown in **Fig. 1a** are obtained from DFT calculations, and the corresponding optimization settings are provided in Section 2.2.

The most stable composition is Na_2ZrO_3 (ΔG_f =-875 meV/metal atom). Its primitive cell consists of two Na_2ZrO_3

Please do not adjust margins

Please do not adjust margins

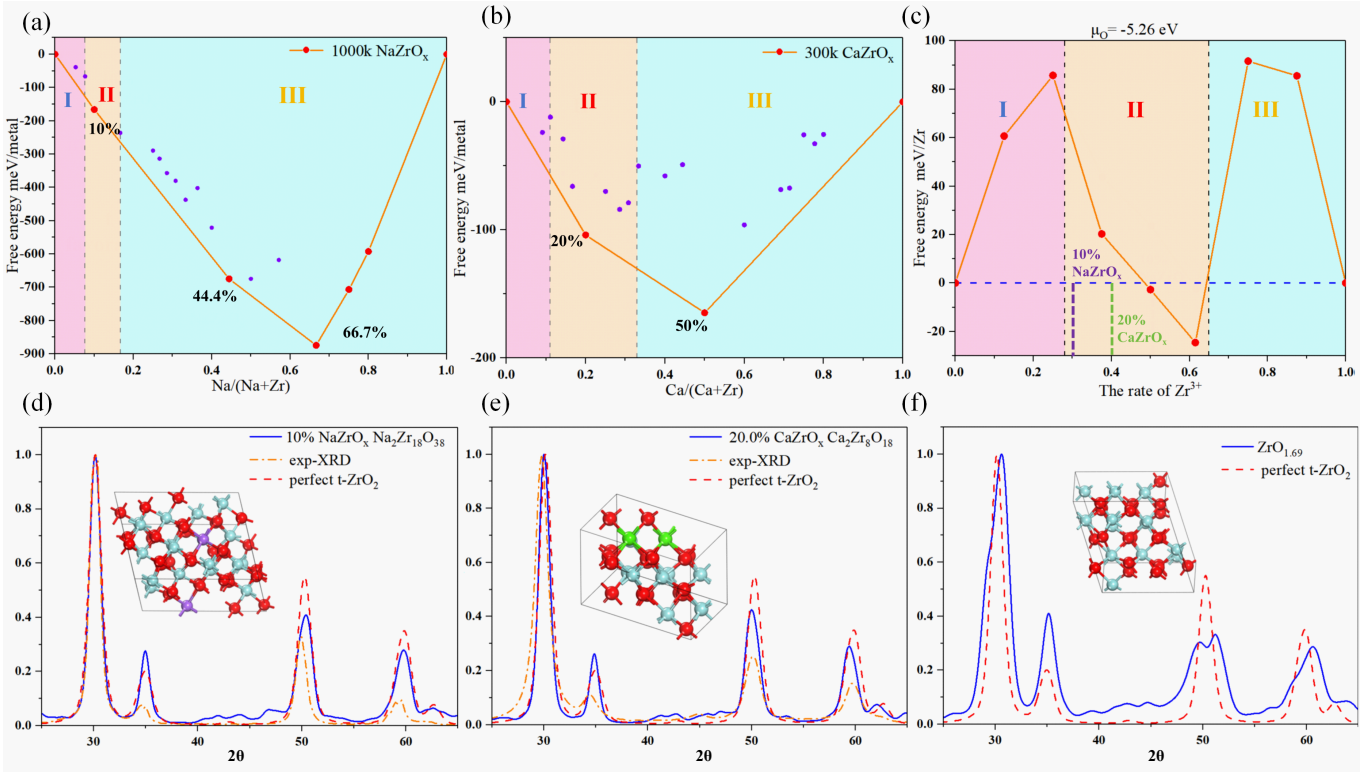

Fig. 1. (a-c) Thermodynamic convex-hull plots for three systems, NaZrO (a), CaZrO (b), and ZrO_{2-x} (c), constructed under synthesis conditions. The x-axis gives the molar percentage of Na^+, Ca^{2+}, or Zr^{3+}, and the y-axis shows the per-metal-atom Gibbs free formation energy under the corresponding conditions. Each panel is partitioned into regions based on the motif of the GM: region I (pink), m-like domain; region II (orange), t-like domain; and region III, rocksalt-like for NaZrO, perovskite-like for CaZrO, and structures with five-coordinated oxygen for ZrO_{2-x}. The orange line connects red points marking GM structures on the hull; purple points denote off-hull, thermodynamically unstable structures. (d-f) Simulated XRD patterns for 10% NaZrO (d), 20% CaZrO (e), and $ZrO_{1.69}$ (f), computed with a line width of 1 over 2θ = 20–70°. Blue curves are simulated patterns, orange curves are experimental spectra, and red curves correspond to the ideal tetragonal (t-ZrO_2) pattern. Insets show the associated structural models: red spheres, O; cyan, Zr; purple, Na; and green, Ca.

units (space group $Pc/2_1$ #14), exhibiting a rock-salt motif, with alternating [Na] and [NaZrO] layers (**Fig. S3**). All Zr atoms are six-coordinated in regular octahedra, consistent with previous experimental observations.[41,42] Other vertex structures with higher Na content (44.4%, 75%, and 80% Na content) display similar rock-salt-like features, forming a structural family that we mark as the blue region in **Fig. 1a**.

Crucially, the convex hull identifies $Na_2Zr_{18}O_{37}$ (10% Na, ΔG_f= -166 meV/metal atom) retaining the t-ZrO_2 motif, which aligns with the experimental observation that NaOH-precipitated t-ZrO_2 typically contains less than 13% Na.[11] Temperature-dependent hulls further reveal that 700 K is the critical threshold at which this composition achieves hull stability (**Fig. 1a**). $Na_2Zr_{18}O_{37}$ is not located on the thermodynamic convex hull at room temperature and only becomes stable on the convex hull at temperatures up to 700 K (close to the amorphous-to-tetragonal transition temperature reported in the literature[13]), as shown in **Fig. S4**. Structurally, all oxygen atoms in $Na_2Zr_{18}O_{37}$ are four-coordinated. The simulated XRD pattern (**Fig. 1d**) reproduces the characteristic peaks at 2θ = 30, 35, 50, and 60°, in excellent agreement with experimental data.[11] Simulated XRD patterns are calculated from optimized static structures using LASPAI (www.laspai.com)[43]. Both Na atoms are eight-coordinated, while substitution of Zr sites by Na^+ introduces 7.5% formal O_v. Consequently, two Zr atoms are eight-coordinated and the rest are seven-coordinated. Radial distribution function (RDF) analysis is performed from molecular dynamics (MD) simulation at 300 K (**Fig. 2**). The MD simulations are carried out using the Nosé–Hoover thermostat and a Parrinello–Rahman barostat for temperature and pressure control (NPT ensemble)[44,45] for a total simulation time of 60 ps with a time step of 0.5 fs. The results confirm that O_v are predominantly associated with Zr atoms, with the first O_v–Zr peaks at 2.45 Å, while O_v–Na and O_v–O_v correlations appear only at longer distances, being 4.28 Å and 5.77 Å, respectively. This suggests that the O_v are isolated and effectively stabilize the local coordination environment of Zr.

We then compare the lowest-energy m-like and t-like structures across different compositions. The results indicate that t-ZrO_2-like structures are energetically favored in the range of 7.7–16.7% Na (yellow region in **Fig. 1a**), whereas m-like structures dominate below 7.7% (pink region in **Fig. 1a**). For example, $Na_2Zr_{36}O_{73}$ (5.3% Na) adopts an m-like motif with Zr

This journal is © The Royal Society of Chemistry 20xx

Please do not adjust margins

Please do not adjust margins

and Na coordination numbers of 7 and 5, respectively (**Fig. S5a**). The simulated XRD (**Fig. S5b**) matches both experimental data for 5.3% NaZrO and the characteristic diffraction of m-ZrO_2[11].

The investigation is then extended to the K_2O-ZrO_2 (KZrO) system, where all convex hull vertices similarly correspond to rock-salt motifs at 1000 K (cyan region, **Fig. S6a**). However, the t-like GM structures occupy a narrower window (11.1–14.3% K component, yellow area in **Fig. S6a**). Unlike the NaZrO system, the KZrO system does not exhibit a t-shaped thermodynamic convex-hull feature between 300 and 1000 K, as shown in **Fig. S6b**. The representative structure nearest the hull, $K_2Zr_{16}O_{33}$ (**Fig. S7a**), lies 39 meV/metal atom above the convex hull edge at 1000 K, suggesting its accessibility as a metastable phase in nanoparticles as reported experimentally[13]. Its simulated XRD (**Fig. S7b**) closely resembles that of t-ZrO_2. Interestingly, the RDF indicates that O_v are distributed around both K and Zr (**Fig. S8**), which likely contributes to its higher formation energy relative to $Na_2Zr_{18}O_{37}$.

3.2 Phase Stability of Alkaline Earth Metal–ZrO_2 Systems

We next extend our methodology to alkaline-earth-doped zirconia, taking CaO-ZrO_2 (CaZrO) as a representative case. SSW sampling is performed across the full compositional range, and the resulting 300 K thermodynamic phase diagram is presented in **Fig. 1b** (also see **Table S7**). In contrast to NaZrO, the CaZrO convex hull exhibits negligible temperature dependence between 300 K and 1000 K (**Fig. S9**), with two stable vertices at 20% and 50% Ca. The most stable convex-hull vertex corresponds to $CaZrO_3$ (50% Ca, ΔG_f=-165 meV/metal atom), consistent with experimental phase diagrams[46]. Its primitive cell (space group Pnma, #62) contains four $CaZrO_3$ units and adopts a distorted perovskite structure related to $CaTiO_3$, featuring alternating [CaO] and [ZrO_2] layers. All O atoms are four-coordinated, while Ca and Zr occupy distorted octahedra (**Fig. S10**). For compositions exceeding 33.3% Ca, the global minimum (GM) structures consistently retain this perovskite-like motif (blue region, **Fig. 1b**).

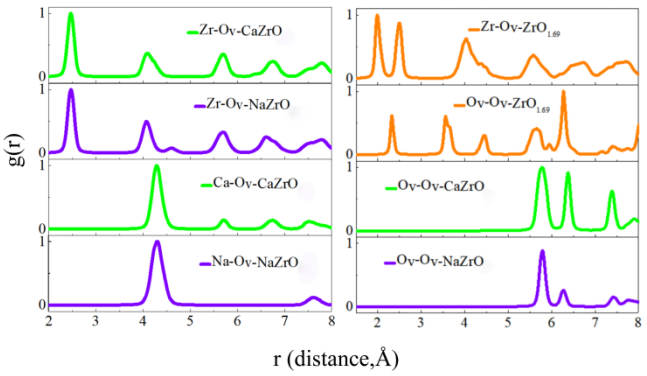

Fig. 2. Radial distribution function (RDF) plots for three different systems. Green line: $Ca_2Zr_8O_{18}$, purple line: $Na_2Zr_{18}O_{37}$, orange line: $ZrO_{1.69}$. The x-axis represents the distance in Å, and the y-axis represents the normalized radial distribution function values.

Similar to NaZrO, the vertex at 20% Ca content ($CaZr_4O_9$) stabilizes the t-ZrO_2 motif (ΔG_f = -95 meV/metal atom). The primitive cell contains two $CaZr_4O_9$ formula units and adopts space group P1. The lattice disorder arises from the introduction of 10% formal O_v, where two Ca atoms form a Ca–Ca dimer (3.61 Å) that is eightfold coordinated, while Zr centers adopt seven-fold coordination. The simulated XRD (**Fig. 1e**) reproduces the characteristic tetragonal reflections at $2\theta \approx 30°$, 35°, 50°, and 60°, in good agreement with both bulk t-ZrO_2 and experimental data for this composition.[9]

RDF analysis of $CaZr_4O_9$ shows a similar O_v distribution to that of the $Na_2Zr_{18}O_{37}$ (**Fig. 2**). The O_v preferentially localizes near Zr, with first-shell distances of 2.45 Å. The first-shell distances of O_v–Ca and O_v–O_v appear at 4.28 Å and 5.77 Å, respectively. Compared with Na, Ca doping exhibits more peaks in the O_v-Ca RDF, indicating less ordered vacancy spacing. Overall, t-like phases dominate between 11.1% and 33.3% Ca concentration (yellow region, **Fig. 1b**), while m-like phases prevail at lower Ca concentration (pink region), being consistent with experimental observations[9,24]. For example, a Ca content of 9.1% corresponds to the $CaZr_{10}O_{21}$ phase, whose structure is shown in **Fig. S10**.

We further apply the same methodology to the MgZrO system (**Fig. S11a**). In contrast to Na- and Ca-doped zirconia, all MgZrO global minima exhibit positive formation energies on the potential-energy surface. Only a single phase, $Mg_4Zr_4O_{12}$ (space group Pnma, #62), emerges on the 300 K free energy surface, with a formation energy of -9 meV/metal atom. Structurally, Zr is seven-coordinated, resembling its environment in m-ZrO_2, while Mg is five-coordinated. Other low-Mg compositions preferentially form m-ZrO_2/MgO interfacial motifs, indicating that Mg incorporation does not effectively stabilize the tetragonal phase.

3.3 Phase Stability of HZrO System

We next examine the potential role of bulky OH^- species in stabilizing tetragonal ZrO_2, which may be incorporated during NH_4OH-assisted synthesis. From the perspective of charge compensation, the incorporation of H^+ as a monovalent cation inherently introduces formal oxygen vacancies O_v into the bulk lattice, operating via a mechanism identical to that of alkali metal dopants. To this end, we examine the phase stability of the H_2O–ZrO_2 (HZrO) system by replacing $Na_2Zr_{18}O_{37}$ with $H_2Zr_{18}O_{37}$. SSW sampling reveals that the GM structures at all H concentrations correspond to OH-terminated m-ZrO_2. However, incorporation of H into the bulk reduces the energetic preference for the m-phase. The smallest m-t energy gap occurs for $H_2Zr_{18}O_{37}$, where the difference decreases from 130 meV per f.u. in pure ZrO_2 to 91 meV per f.u. Free-energy evaluations of m-like and t-like structures (**Table S9**) further demonstrate that the t-like $H_2Zr_{18}O_{37}$ structure becomes thermodynamically favored above 968 K whereas pure t-ZrO_2 becomes more stable than m-ZrO_2 only at 1453 K.

Structural analysis of $H_2Zr_{18}O_{37}$ (**Fig. S12**) reveals a lattice where Zr atoms are predominantly seven-coordinated (16 sites) with two eight-coordinated sites. The oxygen species comprise 2 OH groups, 26 four-coordinated O atoms, and 9 three-

Please do not adjust margins

Please do not adjust margins

coordinated O atoms. The simulated XRD exhibits characteristic tetragonal reflections at 2θ ≈ 30°, 35°, 50°, and 60°. Several experimental observations indicate that, during the calcination of t-ZrO_2 synthesized using aqueous ammonia, a decrease in water content is often accompanied by a phase transformation.[47]

3.4 Phase Stability of Defective ZrO_{2-x}

Our results from NaZrO, KZrO, CaZrO and HZrO systems collectively demonstrate that the stabilization of the tetragonal phase is driven by the substitution of Zr sites with lower-valence cations. This substitution necessitates the formation of O_v that preferentially localize around Zr atoms, directly perturbing the local Zr–O coordination. For instance, 20%-CaZrO and 10%-NaZrO possess ~10% and 7.5% formal O_v concentrations, respectively. To directly probe the role of oxygen vacancies, we further investigate the thermodynamic phase diagram of the ZrO_{2-x} system ($0 \le x \le 0.50$) from the free energies of ZrO_2 and Zr_2O_3 at 1000 K with an oxygen chemical potential of -5.26 eV (**Fig. 1c**), providing a comprehensive picture of the structural evolution as a function of vacancy concentration.

Thermodynamic analysis reveals three distinct structural regimes governed by the vacancy concentration, x (**Fig. 1c**). For $x \le 0.12$ (region I), the GM structures retain m-like ZrO_2 character. For $x > 0.31$ (region III), the GMs evolve toward Zr_2O_3-like configurations, where half of the oxygen species adopt fivefold trigonal-bipyramidal coordination while the remainder are tetrahedral (blue region in **Fig. 1c**; structure in **Fig. S13**). Within this range, $0.12 < x \le 0.31$ (region II), the GM structures adopt the tetragonal ZrO_2 framework. Notably, the O_v concentrations in 10% NaZrO and 20% CaZrO fall precisely within this "tetragonal window" (**Fig. 1c**), suggesting that O_v density is a primary descriptor for phase stability across disparate synthesis routes.

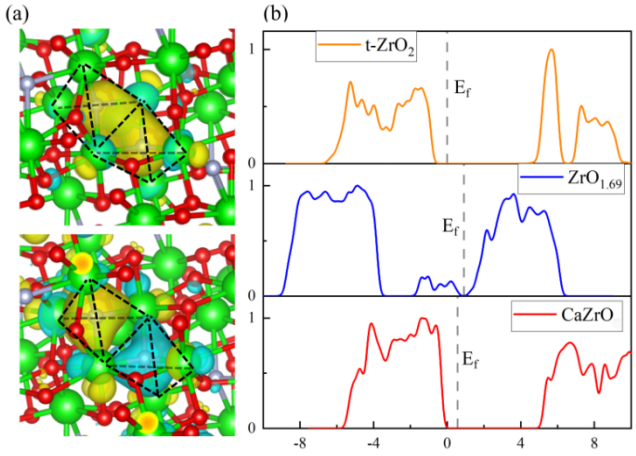

Fig. 3. (a) Real-space wave functions of the HOMO–2 (bottom) and HOMO–3 (top) orbitals for $ZrO_{1.69}$; yellow and cyan indicate the opposite signs of the wave functions. Zr atoms are shown in green and O atoms in red. (b) Total density of states (DOS) for three systems: t-ZrO_2 (orange), $ZrO_{1.69}$ (blue), and 20% CaZrO (red). The x-axis denotes energy, referenced to the Fermi level of t-ZrO_2 set to 0 eV and aligned across systems by matching the Zr 4s level; the y-axis gives the total DOS.

At $x = 0.31$ ($ZrO_{1.69}$), the formation energy reaches –23 meV per Zr atom, being the only vertex on the phase diagram. This composition, corresponding to $Zr_{13}O_{22}$, incorporates four oxygen vacancies relative to stoichiometric $Zr_{13}O_{26}$ in the primitive cell. Six Zr sites that are adjacent to the vacancies exhibit reduced coordination numbers of 5–6, whereas the remaining seven Zr atoms are 7-coordinate. The oxygen sublattice contains 3-fold and 4-fold coordinated O in a ratio of 3:8. The local configuration (**Fig. 1f**) reproduces the tetrahedral O coordination characteristic of t-ZrO_2, and its simulated XRD (**Fig. 1f**) shows the tetragonal reflections at 2θ = 30, 35, 50, and 60°.

The Zr-O_v RDF of $ZrO_{1.69}$ displays a unique peak at 2.02 Å alongside the standard peaks at 2.50 Å and 4.05 Å found in MZrO systems. Bader charge analysis (**Table S8**) confirms that this short-range peak arises from the presence of reduced Zr^{3+} species, which effectively reduce the Zr–O vacancy distance. For the O_v–O_v distribution, RDF reveals characteristic peaks at 2.35 and 3.53 Å, corresponding to O_v pairs occupying edge-sharing and corner-sharing tetrahedral ionic voids, respectively (**Fig. 2**).

We analyze the density of states (DOS) of $ZrO_{1.69}$ and compare it with 20% CaZrO and pristine t-ZrO_2 (**Fig. 3**). While CaZrO and pristine t-ZrO_2 show typical insulating gaps of 5.54 and 5.37 eV, the non-stoichiometric $ZrO_{1.81}$ and $ZrO_{1.69}$ exhibit much narrower band gaps of 1.40 and 0.73 eV (the band structures are shown in **Fig. S14**), respectively, consistent with the light-brown color reported experimentally. This narrow gap originates from the presence of oxygen vacancies that inject excess electrons into the lattice, producing mid-gap defect states that effectively reduce the band gap. Wavefunction analysis further identifies the HOMO-2 and HOMO-3 bands as F-center states localized on O_v-O_v pairs within the edge-sharing tetrahedral ionic voids (**Fig. 3**). The orbitals are mainly composed of the d-orbitals of Zr atoms forming this twin vacancy. Specifically, HOMO–3 resembles a σ bonding orbital, while HOMO–2 shows a nodal plane between the two vacancies, akin to a σ-antibonding orbital. This electronic localization not only stabilizes the defective lattice but also imparts targeted optoelectronic functionalities to the tetragonal phase.

3.5 Prediction of Doped Zirconia Systems

Thermodynamic analysis of the MZrO systems (M = other metals) indicates that the stability of O_v around Zr atoms is a key descriptor governing the formation of stable tetragonal (t-phase) solid solutions. In systems such as $Na_2Zr_{18}O_{37}$ and $CaZr_4O_9$, vacancies preferentially localize around Zr, facilitating the tetragonal framework. Conversely, in the MgZrO system, vacancies are sequestered by the Mg^{2+} dopant, precluding t-phase stabilization. KZrO represents an intermediate case, in which oxygen vacancies are distributed around both K and Zr sites, resulting in only moderate stabilization where the t-phase is accessible but thermodynamically less robust than in NaZrO.

Based on this insight, we develop a unified framework to evaluate whether elements with common oxidation states (I, II, and III) can promote the formation of t-MZrO solid solutions. Starting from the primitive cell of t-ZrO_2, a 2×2×2 supercell

This journal is © The Royal Society of Chemistry 20xx

Please do not adjust margins

Please do not adjust margins

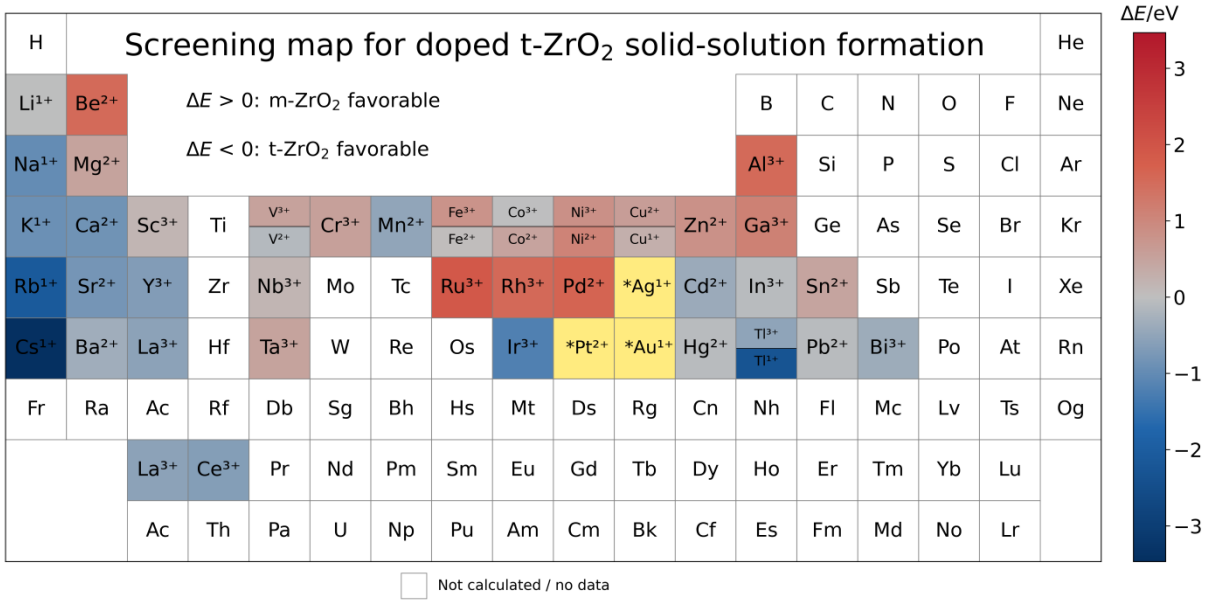

Fig. 4. Screening map of the descriptor $\Delta E = E_2 - E_1$ for t-ZrO_2 solid-solution formation across periodic-table elements with common oxidation states (I–III). Values are obtained from SSW-NN/DFT on a 2×2×2 t-ZrO_2 supercell where corner/body-center Zr atoms are substituted by M; E_1 and E_2 are the total energies with an O vacancy near M and near Zr, respectively. Positive ΔE (>0) means vacancies prefer M (disfavoring stabilization of t-ZrO_2), while negative ΔE (<0) means vacancies localize near Zr (favoring stabilization). Horizontal lines inside the grid separate oxidation states. Color scale: red = positive ΔE; blue = negative ΔE; darker shades = larger magnitude; gray = $\Delta E \approx 0$; white boxes = not calculated. Asterisked yellow boxes (*) mark Pt, Ag, and Au: the structures exhibit strong distortion away from the original t-phases after element replacement due to the preference of the two-fold coordination environment of dopant metal cations.

model is constructed, in which we substitute Zr sites with a dopant metal M in various oxidation states (I, II, and III). Oxygen vacancies are then introduced either around M or around Zr, with their specific positions described in the Supporting Information. All structures are optimized using DFT. The total energies of configurations with O_v near M and Zr are denoted as E_1 and E_2, respectively. The difference $\Delta E = E_2 - E_1$ serves as a descriptor for assessing the dopant's ability to stabilize t-ZrO_2 solid solutions. A negative ΔE indicates that vacancies localize near Zr, stabilizing the t-ZrO_2 lattice, while a positive ΔE indicates vacancy trapping by the dopant, which destabilizes the t-phase. The ΔE values are presented as a predictive heatmap (**Fig. 4**), where red and blue denote positive and negative ΔE values, respectively (with darker shades indicating larger magnitudes), gray indicates ΔE values near zero, and white boxes represent uncalculated cases.

The screened and computed metal oxides fall into three groups. Group I covers most alkali and alkaline-earth metals (except Li, Be, and Mg)—together with several other cations (Y^{3+}, Ce^{3+}, Mn^{2+}, Ir^{3+}, Cd^{2+}, Tl^{3+}, Tl^{+}, Bi^{3+}). These cations typically adopt eightfold coordination, driving O_v to accumulate around Zr. While many of these are experimentally known, our model predicts that solid solutions are realized experimentally, although t-ZrO_2 solid solutions containing Ir^{3+}, Tl^{3+}, or Tl^{+} are not yet widely reported. Group II is characterized by $\Delta E > 0$ (red squares in **Fig. 4**): here the dopant cations tend to capture oxygen vacancies themselves rather than promote Zr-centered vacancies, rendering the corresponding t-ZrO_2 solid solutions thermodynamically unstable (Zn^{2+}, Fe^{3+}, $Ni^{2,3+}$, Ru^{3+}, Rh^{3+}, Co^{2+}, Cu^{2+}, Cr^{3+}, Al^{3+}, Ga^{3+}, V^{3+}, Be^{2+}, Mg^{2+}). Asterisked yellow boxes (*) denote Pt, Ag, Au, which are two-coordinated after optimization, effectively mimicking a high-vacancy environment. Group III comprises boundary cases (Li^{+}, Hg^{2+}, In^{3+}, Pb^{2+}, V^{2+}, Co^{3+}, Cu^{+}, Fe^{2+}), for which t-MZrO solid solutions may be accessible under suitable thermodynamic conditions (gray in **Fig. 4**). In this region, the structural outcomes are dictated by other geometric parameters, often leading to delicate competition between metastable monoclinic, tetragonal, and cubic phases.[48,49] To further validate the descriptor, we compute the formation energies (E_f) for M substitution, defined relative to t-ZrO_2 and the corresponding bulk M oxides. Plotting E_f against ΔE (**Fig. S15**) reveals an approximate linear correlation, confirming that dopants with $\Delta E < 0$ are more likely to form thermodynamically stable t-ZrO_2 solid solutions. Tetravalent to hexavalent metal dopants, such as Hf, Nb and W, do not introduce oxygen vacancies in the ZrO_2 lattice. Consistently, both experimental and theoretical literature indicates that these high-valence dopants are incapable of stabilizing the tetragonal phase in the absence of oxygen vacancies.[50–53] We emphasize that ΔE is a 0 K potential-energy criterion intended for the rapid initial screening of candidate dopants. Its transferability across dopant concentrations, oxidation states, vacancy densities, and local structural motifs is only partially explored in the present work, and the phase behavior of real materials can additionally reflect hydrogen incorporation, kinetic trapping, finite-size effects, and synthesis-dependent kinetics, as discussed in Section 4.3.

Please do not adjust margins

Please do not adjust margins

3.6 Experimental Verification

To validate the dominant role of O_v in stabilizing t-ZrO_2, the hybrid sol–gel zirconia (HSGZ) and a reference sample without the addition of acetylacetone (SGZ) are synthesized via an organic-reductant-assisted sol–gel method, following a previously reported procedure[25]. The samples are subsequently calcined at 600 °C under either N_2 (denoted as HSGZ–N_2 and SGZ–N_2) or air (denoted as HSGZ–air and SGZ–air). As revealed by the XRD patterns (**Fig. 5a**), the samples exhibit distinct, atmosphere-dependent phase behaviors. Both N_2-annealed samples retain a pure *t*-ZrO_2 phase. In contrast, calcination in air triggers partial $t \rightarrow m$ phase transformations, leaving HSGZ–air and SGZ–air with tetragonal phase fractions of 75.72% and 33.40%, respectively (estimated using a semi-quantitative RIR method)[54]. Concurrently, the N_2-annealed samples appear black (**Fig. S17**), while the air-annealed samples turn white. The electron paramagnetic resonance (EPR) measurements (**Fig. 5b**) of HSGZ–N_2 display the strongest signal at g = 2.003, which is characteristic of oxygen vacancies,[55] confirming the highest retention of O_v, followed by a weaker signal in SGZ–N_2, whereas SGZ–air shows almost no signal. This gradient in EPR intensity correlates with the phase composition variations in **Fig. 5a:** the high concentration of O_v stabilizes the tetragonal lattice and induces the black coloration, whereas the depletion of O_v under an air atmosphere drives the detrimental $t \rightarrow m$ phase transition.

To evaluate the predictive capability of our framework, Ir-doped (IrZrO) and Ru-doped (RuZrO) zirconia solid solutions (XIrZrO, XRuZrO, X indicates X mol% dopant amount) are synthesized via a solvothermal method (details in SI). Based on the descriptor heatmap (**Fig. 4**), Ir^{3+} is predicted to stabilize the tetragonal phase, whereas Ru^{3+} induces instability. XRD patterns (**Fig. 5c**) show that 30IrZrO forms a fully tetragonal phase, whereas 30RuZrO and undoped ZrO_2 exhibit mixed phases. Specifically, Ru doping exacerbates the instability of the t-phase, causing its fraction to drop from 39.42% to 30.53%. In addition, the proportion of t-phase gradually increases with increasing Ir doping (**Fig. S19**). Inductively coupled plasma (ICP) analysis confirms that the actual Ir content increases from 3.1% in 5IrZrO to 22.5% in 30IrZrO (**Table S11**). TEM analysis (**Fig. 5d**) reveals clear lattice fringes (0.303 nm) in IrZrO, indicating lattice expansion due to Ir incorporation. Energy Dispersive X-ray Spectroscopy (EDS) mapping (**Fig. S20**) demonstrates that, although Ir agglomerates in some areas, it is generally distributed uniformly, confirming that portions of Ir form solid solutions with Zr. These results validate the descriptor in **Fig. 4** and establish a rational route for designing stabilized tetragonal ZrO_2-based solid solutions.

Finally, the descriptor ΔE is a 0 K potential-energy quantity and does not itself vary with temperature, and the classification it defines therefore remains valid across the experimental temperature range. As evaluated by the ΔE descriptor in Section 3.5 to assess dopant tendencies for *t*-ZrO_2 formation, Mg and Ni exhibit $\Delta E > 0$, theoretically predicting poor thermodynamic stability for the t-phase. Nevertheless, experimentally, t-MgZrO and t-NiZrO can often be obtained under hydrothermal conditions. This metastable capturing is likely driven by synthesis-dependent kinetic factors, such as surface-bound OH groups that temporarily diminish the *t–m* energy barrier. To decouple true thermodynamic stability from such transient processing effects, the hydrothermally prepared t-MgZrO, t-NiZrO, and t-CaZrO samples are calcined at 1100 °C. The XRD patterns (**Fig. S21**) show that t-CaZrO remains tetragonal after calcination, with an average CaZrO nanoparticle size of 43.38 ± 1.11 nm, whereas MgZrO and NiZrO undergo phase transformation, with the behavior of MgZrO being consistent with the MgO–ZrO phase diagram.[56,57] Crucially, the persistent stability at this macroscopic scale solidifies our core thesis that the bulk phase thermodynamics, instead of finite-size surface effects, plays the decisive role.

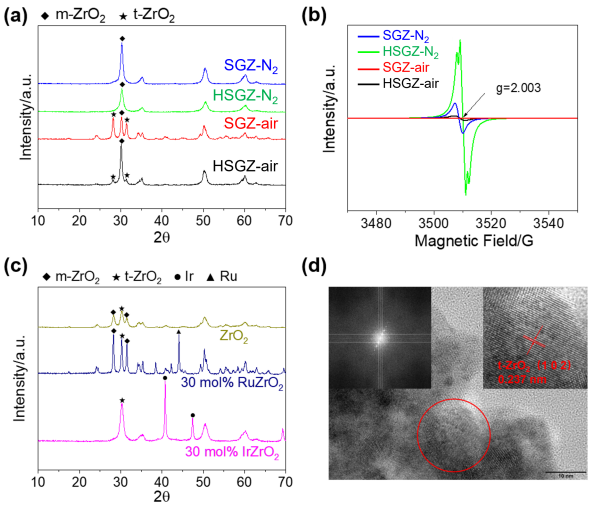

Fig. 5. The XRD (a) and EPR (b) patterns of SGZ and HSGZ. The XRD pattern of RuZrO and IrZrO (c). The TEM image of IrZrO (d).

4. Discussion

4.1 Geometric Origins of Oxygen-Vacancy-Mediated Stabilization

The present results establish a unified, vacancy-centered mechanism governing the stability of t-ZrO_2 and its solid solutions. Across all investigated systems, the formation and distribution of O_v, particularly those localized within the coordination environment of Zr^{4+}, serve as the fundamental chemical lens through which various stabilization routes can be understood. From the perspective of Pauling's rules, structural stability requires a commensurate match between cation–anion radius ratios and coordination environments. For Zr^{4+}, the ionic radius ratio with O^{2-} (0.68) is inherently marginal for ideal eightfold coordination. The introduction of O_v proximal to Zr cations effectively relaxes this geometric constraint by reducing local coordination requirements and alleviating lattice strain. This vacancy-assisted stabilization is intrinsically local and does not necessitate long-range chemical ordering, which explains the ubiquity of the tetragonal phase in nanocrystalline and defect-rich systems, working synergistically with the traditional grain boundary or surface energy constraints.

This journal is © The Royal Society of Chemistry 20xx

Please do not adjust margins

Please do not adjust margins

4.2 Rationalizing Synthesis-Dependent Phase Behavior via the Vacancy Mechanism

This proposed mechanism provides a unified explanation for several long-standing experimental observations. For instance, in the NaZrO system synthesized via hydrothermal treatment, the t-ZrO_2 fraction correlates directly with Na content. Xie et al. observe that decreasing Na content from ~12.5% to ~2.0% during high-temperature calcination (600–800 °C) is accompanied by a rapid t→m phase transition.[11] This confirms that Na volatilization—and the subsequent loss of stabilized vacancies—is the primary driving force for phase reversion. Similarly, our convex hull calculations for the CaZrO system identify $Ca_2Zr_8O_{18}$ as a stable phase, which is in excellent agreement with the experimental thermodynamic phase diagrams reported by Kwon et al.[46] The sensitivity of tetragonal ZrO_2 to the surrounding atmosphere follows naturally from the same mechanism. Increasing temperature promotes oxygen uptake from the environment, which annihilates oxygen vacancies and triggers the t→m transformation near 700 °C.[26] Conversely, lowering oxygen partial pressure suppresses this transition, consistent with experimental observations that vacancy preservation stabilizes the tetragonal phase.[58]

In addition to aliovalent dopants, hydrogen-containing species introduce an additional stabilization channel. In NH_4OH-precipitated systems, the observed mass loss of ~0.4% during calcination-induced t→m transformation[47] closely matches the hydrogen content predicted for the t-$H_2Zr_{18}O_{37}$ configuration identified in this work. This quantitative agreement strongly suggests that many "pure" tetragonal zirconia samples reported in the literature are, in fact, hydroxyl-stabilized ZrO_xH_y species at low temperatures. Hydrogen and hydroxyl groups act synergistically with oxygen vacancies, reducing the m–t energy gap and stabilizing the tetragonal framework until dehydroxylation and oxygen uptake eliminate this stabilization pathway.

4.3 Metastable Nominal Solid Solutions and Protonic Bulk Stabilization

A notable discrepancy arises for dopants with $\Delta E > 0$ (e.g., Zn, Mg, Al, and Ga). While our model predicts that such elements should be intrinsically unable to stabilize bulk t-ZrO_2, tetragonal phases are nevertheless frequently reported experimentally.[59–62] This apparent contradiction can be resolved by distinguishing true thermodynamically stable bulk solid solutions from metastabilities driven by kinetic trapping or alternative defect compensation.

First, instead of achieving homogeneous bulk doping, these systems often form phase-separated or kinetically frozen domains that appear tetragonal but are fundamentally metastable. For instance, XPS measurements of nominal "ZnZrO" systems reveal surface Zn concentrations (~30%) nearly twice those of the bulk (~18%),[63] indicating that Zn predominantly forms ZnO-like surface species rather than a homogeneous solid solution. Similar surface enrichment and defect accumulation are reported for GaZrO systems.[62] Global optimization and classical phase diagrams also confirm a lack of stable ZnZrO, NiZrO, AlZrO or MgZrO solid solutions at equilibrium. [56,64,65] Such surface segregation indicates that the synthesized products may not be thermodynamically stable, but rather metastable phases.

Second, bulky protonic (hydroxyl) compensation provides a thermodynamic stabilization channel, operating via a mechanism identical to that of monovalent cations that generate formal oxygen vacancies to maintain charge neutrality. As demonstrated in the HZrO system (Section 3.3), this proton-induced vacancy incorporation behaves in formal analogy to alkaline additives, reducing the monoclinic–tetragonal energy gap and allowing the tetragonal structure to be stabilized.

Taken together, these results highlight that ΔE serves as a necessary but not exclusive descriptor for tetragonal stabilization. While a negative ΔE reliably signals robust bulk stabilization driven by vacancy localization near Zr (Group I), the observed phase behavior of real materials may also reflect contributions from hydrogen incorporation, kinetic trapping, finite-size effects, and synthesis-dependent kinetics. Explicitly accounting for these factors reconciles disparate experimental reports and establishes a unified framework linking bulk thermodynamics with realistic materials chemistry, which is consistent with previous studies on the stability of ZrO_2.[66–69] Finally, the crystallization behavior of $NH_3 \cdot H_2O$-derived zirconia further illustrates the interplay between bulk thermodynamics and kinetics: experimentally, hydrothermally prepared amorphous precursors crystallize into t-ZrO_2 upon calcination at only 673–773 K,[70] about 200–300 K below the bulk threshold predicted for $H_2Zr_{18}O_{37}$ (968 K, Section 3.3), indicating that crystallization initiates in the smallest nanocrystals — where the tetragonal phase is additionally stabilized by surface energetics — and is subject to kinetic control.

5. Conclusions

In summary, this work provides a comprehensive thermodynamic and physical picture that unravels the long-standing mystery of tetragonal ZrO_2 phase stabilization under mild conditions. By utilizing the SSW-NN global potential energy surface exploration, we successfully map the thermodynamic convex hulls of representative alkali, alkaline-earth, and rare-earth metal–zirconia systems. Our results demonstrate that formal oxygen vacancies (O_v) act as an omnipresent thermodynamic baseline that persists across all regimes. Crucially, as verified by our experimental synthesis of stable CaZrO with a macroscopic grain size of ~43 nm, the intrinsic bulk properties governed by vacancy chemistry take over as the decisive driving force dictating the macroscopic phase boundaries.

Electronically, we confirm that vacancy–vacancy interactions give rise to F-center-like defect states within the band gap, lowering the energetic penalty of tetragonal coordination and providing an atomistic explanation for the phase transition. Driven by this bulk coordination chemistry, we establish a physically transparent descriptor ΔE derived from the localized lattice relaxation around O_v. Through high-throughput screening of over 40 dopant candidates, a previously unreported, highly stable IrZrO tetragonal solid solution is successfully predicted and validated by experimental synthesis.

This journal is © The Royal Society of Chemistry 20xx

Please do not adjust margins

Please do not adjust margins

Importantly, our framework provides a unified, vacancy-centered perspective that connects disparate experimental phenomena. We demonstrate that whether driven by intentional metal doping or wet-chemical proton H^+ incorporation, the underlying physical origin of tetragonal stabilization consistently converges on the specific spatial distribution and density of formal bulk oxygen vacancies. Ultimately, by bridging macroscopic thermodynamics with microscopic defect engineering, this work advances the field from empirical trial-and-error toward the rational, theory-guided design of functional metastable solid solutions.

Author contributions

Z.-P. L. and C. S. conceive the project and contribute to the study design and data analysis. Z.-Z. H. performs most of the calculations and writes the original draft of the manuscript. T.-F. L. carries out the experimental work. All authors discuss the results and review and comment on the manuscript.

Conflicts of interest

There are no conflicts to declare.

Data availability

The data supporting this article are included as part of the ESI.

Acknowledgements

This work is supported by the National Key Research and Development Program of China (2025YFA1510900, 2024YFA1509600), the National Science Foundation of China (12188101, U25B6005, 22033003, 92472113), the Fundamental Research Funds for the Central Universities (20720250005, 20720220011), the robotic AI-Scientist platform of Chinese Academy of Science, and the Tencent Foundation for XPLORER PRIZE. The computations in this research are performed using the CFFF platform of Fudan University.

References

1 K. Yuan, Y. Yamazaki, X. Jin and K. Nozaki, Multifunctional WO_3 –ZrO_2 -Supported Platinum Catalyst for Remarkably Efficient Hydrogenolysis of Esters to Alkanes, *J. Am. Chem. Soc.*, 2023, **145**, 3454–3461.

2 D. Kordus, S. Widrinna, J. Timoshenko, M. Lopez Luna, C. Rettenmaier, S. W. Chee, E. Ortega, O. Karslioglu, S. Kühl and B. Roldan Cuenya, Enhanced Methanol Synthesis from CO_2 Hydrogenation Achieved by Tuning the Cu–ZnO Interaction in ZnO/Cu_2 O Nanocube Catalysts Supported on ZrO_2 and SiO_2, *J. Am. Chem. Soc.*, 2024, **146**, 8677–8687.

3 X. Zhang, A. V. Kirilin, S. Rozeveld, J. H. Kang, G. Pollefeyt, D. F. Yancey, A. Chojecki, B. Vanchura and M. Blum, Support Effect and Surface Reconstruction in In_2O_3 / *m*- ZrO_2 Catalyzed CO_2 Hydrogenation, *ACS Catal.*, 2022, **12**, 3868–3880.

4 Y. Chen, J. Tan, J. Sun, H. Guo, J. Bai, P. Zhou, D. Zhang and G. Liu, Effect of sintering temperature on the microstructures and mechanical properties of ZrO2 ceramics fabricated by additive manufacturing, *Ceramics International*, 2024, **50**, 11392–11399.

5 S. Huang, H. Wu, C. Jiang, X. Fu, Y. Liu, J. Zhang, L. He, P. Yang, X. Deng and S. Wu, Preparation of high-strength ZrO2 ceramics by binder jetting additive manufacturing and liquid glass infiltration, *Ceramics International*, 2024, **50**, 44175–44185.

6 L. Fan, C. Huang, H. Liu, Z. Wang, L. Xu, S. Huang, M. Qu, Z. Xu, S. Li and S. Xu, The effect of ZrO2 particle size and solid loading on the rheological properties of highly thixotropic ZrO2 ceramic slurries applied in photopolymerization 3D printing, *Ceramics International*, 2025, **51**, 6669–6678.

7 B. Qi, S. Liang, Y. Li, C. Zhou, H. Yu and J. Li, ZrO_2 Matrix Toughened Ceramic Material-Strength and Toughness, *Adv Eng Mater*, 2022, **24**, 2101278.

8 S. Shukla and S. Seal, Thermodynamic Tetragonal Phase Stability in Sol−Gel Derived Nanodomains of Pure Zirconia, *J. Phys. Chem. B*, 2004, **108**, 3395–3399.

9 S. Liu, Z. Song, J. Wang, B. Han and Y. Sun, In situ self-assembly preparation and characterization of CaO–ZrO2 nanopowders under vacuum, *Vacuum*, 2023, **213**, 112089.

10 J. Chen, Z. Cai, X. Chen, X. Zheng and Y. Zheng, Facile synthesis of ordered mesoporous CaO-ZrO2 composite with mild conditions, *Materials Letters*, 2016, **168**, 214–217.

11 H. Xie, J. Lu, M. Shekhar, J. W. Elam, W. N. Delgass, F. H. Ribeiro, E. Weitz and K. R. Poeppelmeier, Synthesis of Na-Stabilized Nonporous t-ZrO_2 Supports and Pt/t-ZrO_2 Catalysts and Application to Water-Gas-Shift Reaction, *ACS Catal.*, 2013, **3**, 61–73.

12 C. Yang, Z. Jin, X. Chen, J. Fan, M. Qiu, K. Fu and Y. Fan, Modified wet chemical method synthesis of nano-ZrO2 and its application in preparing membranes, *Ceramics International*, 2021, **47**, 13432–13439.

13 H. Wang, G. Li, Y. Xue and L. Li, Hydrated surface structure and its impacts on the stabilization of t-ZrO2, *Journal of Solid State Chemistry*, 2007, **180**, 2790–2797.

14 R. C. Garvie and M. F. Goss, Intrinsic size dependence of the phase transformation temperature in zirconia microcrystals, *J Mater Sci*, 1986, **21**, 1253–1257.

15 Y. Peng, X.-L. Si, C. Shang and Z.-P. Liu, Abundance of Low-Energy Oxygen Vacancy Pairs Dictates the Catalytic Performance of Cerium-Stabilized Zirconia, *J. Am. Chem. Soc.*, 2024, **146**, 10822–10832.

16 S.-H. Guan, K.-X. Zhang, C. Shang and Z.-P. Liu, Stability and anion diffusion kinetics of Yttria-stabilized zirconia resolved from machine learning global potential energy surface exploration, *The Journal of Chemical Physics*, 2020, **152**, 094703.

17 S. Fabris, A stabilization mechanism of zirconia based on oxygen vacancies only, *Acta Materialia*, 2002, **50**, 5171–5178.

18 S. Chang and R. Doong, Chemical-Composition-Dependent Metastability of Tetragonal ZrO_2 in Sol−Gel-Derived Films under Different Calcination Conditions, *Chem. Mater.*, 2005, **17**, 4837–4844.

19 S. Shukla and S. Seal, Mechanisms of room temperature metastable tetragonal phase stabilisation in zirconia, *International Materials Reviews*, 2005, **50**, 45–64.

20 W. Piskorz, J. Gryboś, F. Zasada, P. Zapała, S. Cristol, J.-F. Paul and Z. Sojka, Periodic DFT Study of the Tetragonal ZrO_2 Nanocrystals: Equilibrium Morphology Modeling and Atomistic Surface Hydration Thermodynamics, *J. Phys. Chem. C*, 2012, **116**, 19307–19320.

21 W. Piskorz, J. Gryboś, F. Zasada, S. Cristol, J.-F. Paul, A. Adamski and Z. Sojka, Periodic DFT and Atomistic Thermodynamic Modeling of the Surface Hydration Equilibria and Morphology of Monoclinic ZrO_2 Nanocrystals, *J. Phys. Chem. C*, 2011, **115**, 24274–24286.

 This journal is © The Royal Society of Chemistry 20xx

Please do not adjust margins

Please do not adjust margins

22 Y. Ding, Z. Wang, Y. Guo, Y. Guo, L. Wang and W. Zhan, A novel method for the synthesis of CexZr1-xO2 solid solution with high purity of κappa phase and excellent reactive activity, *Catalysis Today*, 2019, **327**, 262–270.

23 B. Butz, P. Kruse, H. Stormer, D. Gerthsen, A. Muller, A. Weber and E. Iverstiffee, Correlation between microstructure and degradation in conductivity for cubic Y2O3-doped ZrO2, *Solid State Ionics*, 2006, **177**, 3275–3284.

24 X. Zhang, S. Wei, X. Zhao, Z. Chen, H. Wu, P. Rong, Y. Sun, Y. Li, H. Yu and D. Wang, Preparation of mesoporous CaO-ZrO2 catalysts without template for the continuous synthesis of glycerol carbonate in a fixed-bed reactor, *Applied Catalysis A: General*, 2020, **590**, 117313.

25 C. Imparato, M. Fantauzzi, C. Passiu, I. Rea, C. Ricca, U. Aschauer, F. Sannino, G. D'Errico, L. De Stefano, A. Rossi and A. Aronne, Unraveling the Charge State of Oxygen Vacancies in ZrO_{2-x} on the Basis of Synergistic Computational and Experimental Evidence, *J. Phys. Chem. C*, 2019, **123**, 11581–11590.

26 S. Kumar and A. K. Ojha, Oxygen vacancy induced photoluminescence properties and enhanced photocatalytic activity of ferromagnetic ZrO2 nanostructures on methylene blue dye under ultra-violet radiation, *Journal of Alloys and Compounds*, 2015, **644**, 654–662.

27 C. Shang, X.-J. Zhang and Z.-P. Liu, Stochastic surface walking method for crystal structure and phase transition pathway prediction, *Phys. Chem. Chem. Phys.*, 2014, **16**, 17845–17856.

28 C. Shang and Z.-P. Liu, Stochastic Surface Walking Method for Structure Prediction and Pathway Searching, *J. Chem. Theory Comput.*, 2013, **9**, 1838–1845.

29 S. Huang, C. Shang, P. Kang, X. Zhang and Z. Liu, LASP: Fast global potential energy surface exploration, *WIREs Comput Mol Sci*, 2019, **9**, e1415.

30 T. Guan, C. Shang and Z.-P. Liu, Local-Softening Stochastic Surface Walking for Fast Exploration of Corrugated Potential Energy Surfaces, *J. Chem. Theory Comput.*, 2024, **20**, 11093–11104.

31 X.-T. Xie, Z.-X. Yang, D. Chen, Y.-F. Shi, P.-L. Kang, S. Ma, Y.-F. Li, C. Shang and Z.-P. Liu, LASP to the Future of Atomic Simulation: Intelligence and Automation, *Precision Chemistry*, 2024, **2**, 612–627.

32 S.-D. Huang, C. Shang, X.-J. Zhang and Z.-P. Liu, Material discovery by combining stochastic surface walking global optimization with a neural network, *Chem. Sci.*, 2017, **8**, 6327–6337.

33 S.-D. Huang, C. Shang, P.-L. Kang and Z.-P. Liu, Atomic structure of boron resolved using machine learning and global sampling, *Chem. Sci.*, 2018, **9**, 8644–8655.

34 P.-L. Kang, Z.-X. Yang, C. Shang and Z.-P. Liu, Global Neural Network Potential with Explicit Many-Body Functions for Improved Descriptions of Complex Potential Energy Surface, *J. Chem. Theory Comput.*, 2023, **19**, 7972–7981.

35 G. Kresse and J. Furthmüller, Efficient iterative schemes for *ab initio* total-energy calculations using a plane-wave basis set, *Phys. Rev. B*, 1996, **54**, 11169–11186.

36 G. Kresse and D. Joubert, From ultrasoft pseudopotentials to the projector augmented-wave method, *Phys. Rev. B*, 1999, **59**, 1758–1775.

37 J. P. Perdew, K. Burke and M. Ernzerhof, Generalized Gradient Approximation Made Simple, *Phys. Rev. Lett.*, 1996, **77**, 3865–3868.

38 S. Grimme, J. Antony, S. Ehrlich and H. Krieg, A consistent and accurate *ab initio* parametrization of density functional dispersion correction (DFT-D) for the 94 elements H-Pu, *The Journal of Chemical Physics*, 2010, **132**, 154104.

39 J. Heyd, G. E. Scuseria and M. Ernzerhof, Hybrid functionals based on a screened Coulomb potential, *The Journal of Chemical Physics*, 2003, **118**, 8207–8215.

40 V. Wang, N. Xu, J.-C. Liu, G. Tang and W.-T. Geng, VASPKIT: A user-friendly interface facilitating high-throughput computing and analysis using VASP code, *Computer Physics Communications*, 2021, **267**, 108033.

41 J. Lee, S. Y. Kwon and I.-H. Jung, Phase diagram study and thermodynamic assessment of the Na2O-ZrO2 system, *Journal of the European Ceramic Society*, 2021, **41**, 7946–7956.

42 H. Näfe and N. Karpukhina, Na-Modified Cubic Zirconia—Link Between Sodium Zirconate and Zirconia in the Na_2O–ZrO_2 Phase Diagram, *Journal of the American Ceramic Society*, 2007, **90**, 1597–1602.

43 Z.-P. L. Han-Zhi Luo Qi-Ming Liang, Zi-Xing Guo, Xin-Tian Xie, Jin-Peng Tang, Tong Guan, Ye-Fei Li, Si-Cong Ma, Ying-Chen Xu, Zhen-Xiong Wang, Cheng Shang, LASPAI: AI-powered platform for the future atomic simulation, *Acta Physico-Chimica Sinica*, 2026, **42**, 100235.

44 W. G. Hoover, Canonical dynamics: Equilibrium phase-space distributions, *Physical Review A*, 3 AD, **31**, 1695–1697.

45 S. Nosé, A unified formulation of the constant temperature molecular dynamics methods, *Journal of Chemical Physics*, 1984, **81**, 511–519.

46 S. Y. Kwon and I.-H. Jung, Critical evaluation and thermodynamic optimization of the CaO-ZrO2 and SiO2-ZrO2 systems, *Journal of the European Ceramic Society*, 2017, **37**, 1105–1116.

47 S. Kumar, S. Bhunia and A. K. Ojha, Effect of calcination temperature on phase transformation, structural and optical properties of sol–gel derived ZrO2 nanostructures, *Physica E: Low-dimensional Systems and Nanostructures*, 2015, **66**, 74–80.

48 L. Liu, C. Li, Y. Chen, X. Zhang, L. Li and Y. Wang, Phase transformation of ZrO2 nanocrystals induced by Li+, *Materials Letters*, 2012, **79**, 75–77.

49 H. Wang, S. Fan, S. Guo, S. Wang, Z. Qin, M. Dong, H. Zhu, W. Fan and J. Wang, Selective conversion of CO2 to isobutane-enriched C4 alkanes over InZrOx-Beta composite catalyst, *Nat Commun*, 2023, **14**, 2627.

50 T. S. Böscke, P. Y. Hung, P. D. Kirsch, M. A. Quevedo-Lopez and R. Ramírez-Bon, Increasing permittivity in HfZrO thin films by surface manipulation, *Applied Physics Letters*, 2009, **95**, 052904.

51 N. Jeon, Propane dehydrogenation over vanadium-doped zirconium oxide catalysts.

52 S.-H. Guan, Y.-F. Li and Z.-P. Liu, Structural Origin for the Enhanced Photocatalysis of Zr$_{1-}$ Ti Oxide Composites from Machine Learning, *J. Phys. Chem. C*, 2023, **127**, 22537–22547.

53 N. Soultanidis, W. Zhou, A. C. Psarras, A. J. Gonzalez, E. F. Iliopoulou, C. J. Kiely, I. E. Wachs and M. S. Wong, Relating *n* -Pentane Isomerization Activity to the Tungsten Surface Density of WO_x /ZrO_2, *J. Am. Chem. Soc.*, 2010, **132**, 13462–13471.

54 Y. Zhang, B. Wang, J. Niu, Z. Qie, R. Zou, R. Cai, J. Huang, S. Xu and X. Fan, On understanding the effect of metal-support interactions on plasma-catalytic CO2 hydrogenation over the Ru/ZrO2 catalysts, *Chemical Engineering Journal*, 2025, **518**, 164799.

55 C. Gionco, M. C. Paganini, E. Giamello, R. Burgess, C. Di Valentin and G. Pacchioni, Paramagnetic Defects in Polycrystalline Zirconia: An EPR and DFT Study, *Chem. Mater.*, 2013, **25**, 2243–2253.

56 D. Pavlyuchkov, D. Dilner, G. Savinykh and O. Fabrichnaya, Phase Equilibria in the ZrO_2 –MgO–MnO_x System, *J. Am. Ceram. Soc.*, 2016, **99**, 3136–3145.

57 I. Saenko and O. Fabrichnaya, Phase Relations in the ZrO2-MgO-FeOx System: Experimental Data and Assessment of

Please do not adjust margins

Please do not adjust margins

Thermodynamic Parameters, *J. Phase Equilib. Diffus.*, 2021, **42**, 254–277.
58 S. Ning, P. Zhan, Q. Xie, Z. Li and Z. Zhang, Room-temperature ferromagnetism in un-doped ZrO_2 thin films, *J. Phys. D: Appl. Phys.*, 2013, **46**, 445004.
59 V. V. Srdić, S. Rakić and Ž. Cvejić, Aluminum doped zirconia nanopowders: Wet-chemical synthesis and structural analysis by Rietveld refinement, *Materials Research Bulletin*, 2008, **43**, 2727–2735.
60 I. Sádaba, M. Ojeda, R. Mariscal, R. Richards and M. López Granados, Preparation and Characterization of Mg-Zr Mixed Oxide Aerogels and Their Application as Aldol Condensation Catalysts, *ChemPhysChem*, 2012, **13**, 3282–3292.
61 Z. Li, Y. Qu, J. Wang, H. Liu, M. Li, S. Miao and C. Li, Highly Selective Conversion of Carbon Dioxide to Aromatics over Tandem Catalysts, *Joule*, 2019, **3**, 570–583.
62 S. Wang, L. Zhang, P. Wang, W. Jiao, Z. Qin, M. Dong, J. Wang, U. Olsbye and W. Fan, Highly selective hydrogenation of CO2 to propane over GaZrOx/H-SSZ-13 composite, *Nat Catal*, 2022, **5**, 1038–1050.
63 M. T. Nikolajsen, J.-C. Grivel, A. Gaur, L. P. Hansen, L. Baumgarten, N. C. Schjødt, U. V. Mentzel, J.-D. Grunwaldt, J. Sehested, J. M. Christensen and M. Høj, Surface Znox on Zirconia is Highly Active for High Temperature Methanol Synthesis, 2023, preprint, DOI: 10.2139/ssrn.4585134.
64 S. M. Lakiza and L. M. Lopato, Stable and Metastable Phase Relations in the System Alumina–Zirconia–Yttria, *Journal of the American Ceramic Society*, 1997, **80**, 893–902.
65 S. Chen, S. Ma and Z.-P. Liu, Zirconia-Supported ZnO Single Layer for Syngas Conversion Revealed from Machine-Learning Atomic Simulation, *J. Phys. Chem. Lett.*, 2021, **12**, 3328–3334.
66 P. Ticali, D. Salusso, R. Ahmad, C. Ahoba-Sam, A. Ramirez, G. Shterk, K. A. Lomachenko, E. Borfecchia, S. Morandi, L. Cavallo, J. Gascon, S. Bordiga and U. Olsbye, CO_2 hydrogenation to methanol and hydrocarbons over bifunctional Zn-doped ZrO_2 /zeolite catalysts, *Catal. Sci. Technol.*, 2021, **11**, 1249–1268.
67 G. Stefanic and S. Music, Factors Influencing the Stability of Low Temperature Tetragonal ZrO2, *Croat. Chem. Acta*, 2002, **75**, 727–767.
68 Y. Deng, C. Wang, X. Xu and H. Li, Machine learning potential for Ab Initio phase transitions of zirconia, *Theoretical and Applied Mechanics Letters*, 2023, **13**, 100481.
69 R. R. C. Mancera, V. S. Vaiss, O. E. E. Espino, R. R. De Avillez, L. G. Appel and L. T. Costa, Zn-doping and oxygen vacancy effects on the reactivity and properties of monoclinic and tetragonal ZrO2: a DFT study, *J Mol Model*, 2022, **28**, 358.
70 Y. Garanin, R. Shakirziyanov, D. Borgekov, N. Volodina, D. Shlimas and M. Zdorovets, Influence of precursors and mineralizers on phase formation in ZrO2 nanoparticles synthesized by the hydrothermal method, *Scientific Reports*, 2025, **15**, 26165.

 This journal is © The Royal Society of Chemistry 20xx

Please do not adjust margins